# Radionuclide identification algorithm for organic scintillator-based radiation portal monitor


## Authors

Marc Paff, Angela Di Fulvio, Shaun Clarke, Sara Pozzi



## Keywords

radiation portal monitor; organic scintillation detector; nuisance alarms; radionuclide identification algorithm; F-scores; spectral angle mapper



## Abstract

We have developed an algorithm for on-the-fly radionuclide identification for radiation portal monitors using organic scintillation detectors. The algorithm was demonstrated on experimental data acquired with our pedestrian portal monitor on moving special nuclear material and industrial sources at a purpose-built radiation portal monitor testing facility. The experimental data also included common medical isotopes. The algorithm takes the power spectral density of the cumulative distribution function of the measured pulse height distributions and matches these to reference spectra using a spectral angle mapper.

F-score analysis showed that the new algorithm exhibited significant performance improvements over previously implemented radionuclide identification algorithms for organic scintillators. Reliable on-the-fly radionuclide identification would help portal monitor operators more effectively screen out the hundreds of thousands of nuisance alarms they encounter annually due to recent nuclear-medicine patients and cargo containing naturally occurring radioactive material. Portal monitor operators could instead focus on the rare but potentially high impact incidents of nuclear and radiological material smuggling detection for which portal monitors are intended.

# 1. Introduction

## 1.1. Motivation

The smuggling of special nuclear material (SNM), including highly enriched uranium (HEU) and weapons-grade plutonium (WGPu), and radiological material across international borders remains a threat to world security [1–11]. The installation of thousands of radiation portal monitors (RPMs) at border crossings, shipping ports, and airports over the past decades aims to detect and deter the movement of these dangerous materials [12–16]. RPMs typically measure gamma ray and neutron count rates. If measured neutron or gamma ray count rates exceed thresholds above the anticipated natural background count rates, the offending vehicle, person, or cargo container undergoes a thorough inspection to determine the location and identity of the radiation source [15,17–20].

Worldwide, only a handful of incidents of nuclear and radiological material interdictions are reported every year [2]. Nevertheless, the Unites States Customs and Border Protection processes hundreds of thousands of RPM radiation alarms annually [15]. Nearly every one of these RPM radiation alarms is a “nuisance” or “innocence” alarm. One major source of nuisance alarms stems from cargo containing a large enough quantity of naturally occurring radioactive material (NORM) to set off the RPM gamma ray alarm. Common NORM culprits include kitty litter, fertilizer, glazed ceramics, and a host of other materials [21]. The second source of nuisance alarms stems from recent nuclear-medicine patients. Depending upon the activity and half-life of the administered isotope, a recent nuclear-medicine patient may alarm at an RPM anywhere from days up to months after a procedure. The medical radionuclide $^{99m}$Tc has a six-hour half-life, and is estimated to retain high enough activity after a procedure to cause an RPM alarm for up to 3.4 days after a procedure. Because $^{99m}$Tc accounts for over 90% of nuclear medicine procedures in the United States, it is also the most common nuisance alarm source amongst nuclear-medicine patients [19].

Nuisance alarms cost additional personnel time and thus financial resources to process [15]. Therefore, RPMs should ideally distinguish special nuclear material from NORM or medical sources on-the-fly. Two challenges hamper this goal. Firstly, measurement times per RPM occupancy are on the order of three seconds, so the collected data can exhibit a high degree of

statistical uncertainty. Secondly, the cost of each RPM unit has to be low enough to make expansive deployment financially feasible.

The vast majority of deployed RPMs contain large slabs of plastic scintillators for gamma ray detection. Organic scintillators would not be the first choice for any spectroscopy application, because Compton scattering is the predominant observed gamma ray detector interaction. High-purity germanium or inorganic scintillators, on the other hand, would exhibit radio-nuclide specific photo-peaks in measured spectra due to the predominant photo-electric effect gamma ray interaction in these detectors. Such detectors could be excellent candidates for an on-the-fly spectroscopic RPM. However, the relatively high cost of these detector materials relative to organic scintillators makes such RPMs unattractive. Therefore, finding a way to use organic scintillator measured pulse height distributions for radionuclide identification would open the door for an affordable spectroscopic RPM.

## 1.2. Past work

We have developed two RPMs using liquid organic scintillation detectors, and tested them on a variety of moving neutron and gamma ray sources with different shielding configurations [22–27]. These RPMs were tested at a purpose-built facility for RPM testing at the European Commission's Joint Research Centre (JRC) in Ispra, Italy, in February and November 2014. A variety of sources, including 51 g of 89.9 % $^{235}$U HEU, and 6.6 g of 93% $^{239}$Pu WGPu, were available to us for testing the RPM response to SNM and other radiation sources.

On-the-fly radionuclide identification was developed in stages for the pedestrian RPM. These identification algorithms relied on template matching between measured and reference gamma ray pulse height distributions (PHDs) [26,28]. The performance of this algorithm was improved with the use of cumulative distribution functions (CDFs) of the pulse height distributions, but none of the algorithms produced the desired close to 100% correct radionuclide identification percentage [26].

# 2. Data analysis method

## 2.1. Raw RPM data

Three seconds of RPM data acquisition are triggered when movement is detected by the occupancy sensors. Detector pulses are digitized and pulse shape discrimination based on a charge integration method is used to discern pulses arising from neutron versus gamma ray interactions in the detectors [29]. Pulse shape discrimination, therefore, allows for the creation of separate PHDs for measured neutron and gamma ray interactions in the RPM. Examples of raw and background-corrected gamma ray PHDs for a moving WGPu source measured with the pedestrian RPM are given in Figure 1. The measured PHDs exhibit high statistical uncertainty due to the low number of counts one can expect in a three second measurement of a moving source of this activity, as seen when comparing the PHDs in Figure 1 before and after background subtraction. Background measurement times were on the order of 30 minutes. Background gamma ray PHDs exhibited low statistical uncertainty relative to the three second moving source measurements.

Each PHD bin on-average contains less than 50 counts after background subtraction. For example, the dataset shown in Figure 1 contains 3556 total counts for a three-second measurement before subtracting a background PHD normalized to three seconds and containing 2062 total counts. Propagating uncertainty for the background subtraction and conversion to count rate result in a combined standard uncertainty of 5% for this single RPM measurement [30]. On-the-fly radionuclide identification therefore is challenging due to this high statistical uncertainty, and due to the lack of radionuclide-specific photopeaks when using organic versus inorganic scintillators.

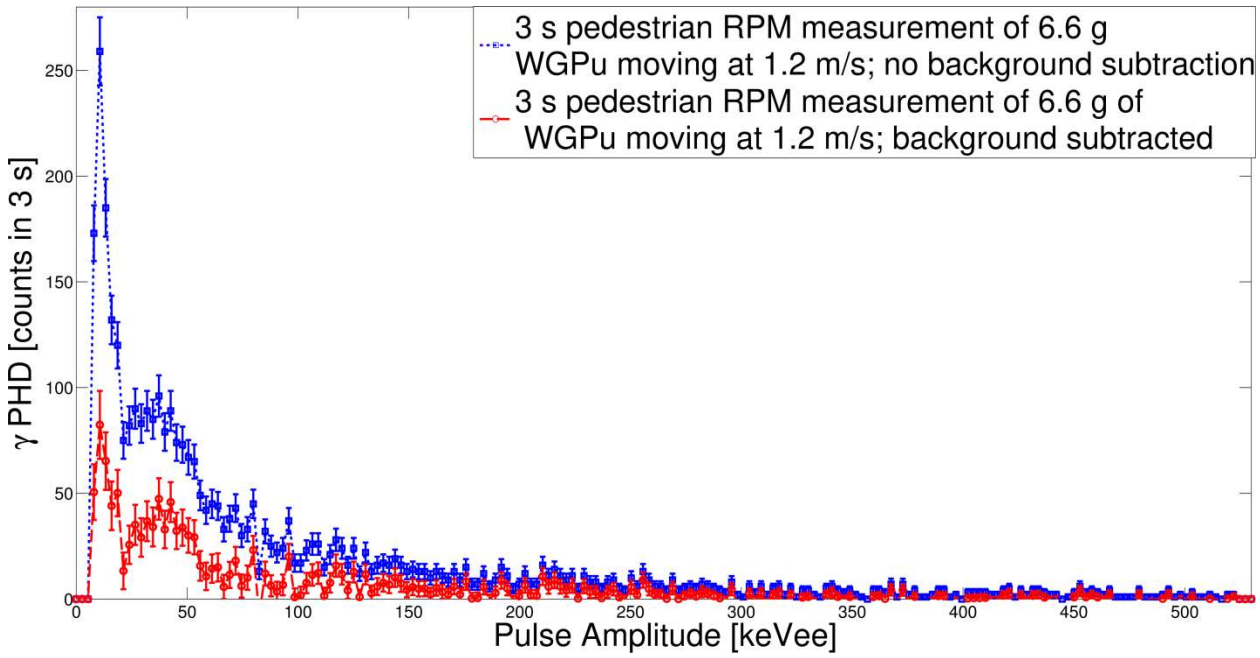


Figure 1: Example of a gamma ray PHD resulting from a three second measurement of moving 6.6 g WGPu with the pedestrian RPM at the European Commission Joint Research Centre in Ispra, Italy, in February 2014 before (blue squares) and after (red circles) background subtraction [26]. The source was moving at 1.2 m/s on an electric rail-cart at 1 m separation from the RPM. The source was travelling at a height of 1.2 m.

## 2.2. Modifying RPM data

The first step in our radionuclide identification algorithm is to compute CDFs of the measured and reference gamma ray PHDs. The CDF, $x(n)$, of any distribution $F_X(x)$ is the probability that X takes a value less than x, i.e., $P(X \leq x)$. A CDF can be computed by integrating the PHD bin-by-bin, and expressing what fraction of the total PHD exists to the left of each bin. Our subsequent analysis uses $y(n) = \big(1 - x(n)\big)$. Figure 2 shows $y(n)$ of 14 gamma ray reference spectra and three moving-source measurements taken with the pedestrian RPM at the JRC and C.S. Mott Children's Hospital [26,27,31]. The x-axis of Figure 2 shows pulse amplitudes in units of light output [keVee] based upon an energy calibration using the Compton edge of $^{137}$Cs. The pulse amplitudes are shown in descending order to better visualize small differences in CDFs at higher energies, whereas much of the CDF arises from only a few lower energy bins, especially in the cases of the lowest energy gamma ray emitting sources, like $^{57}$Co and $^{241}$Am.

**(a)**

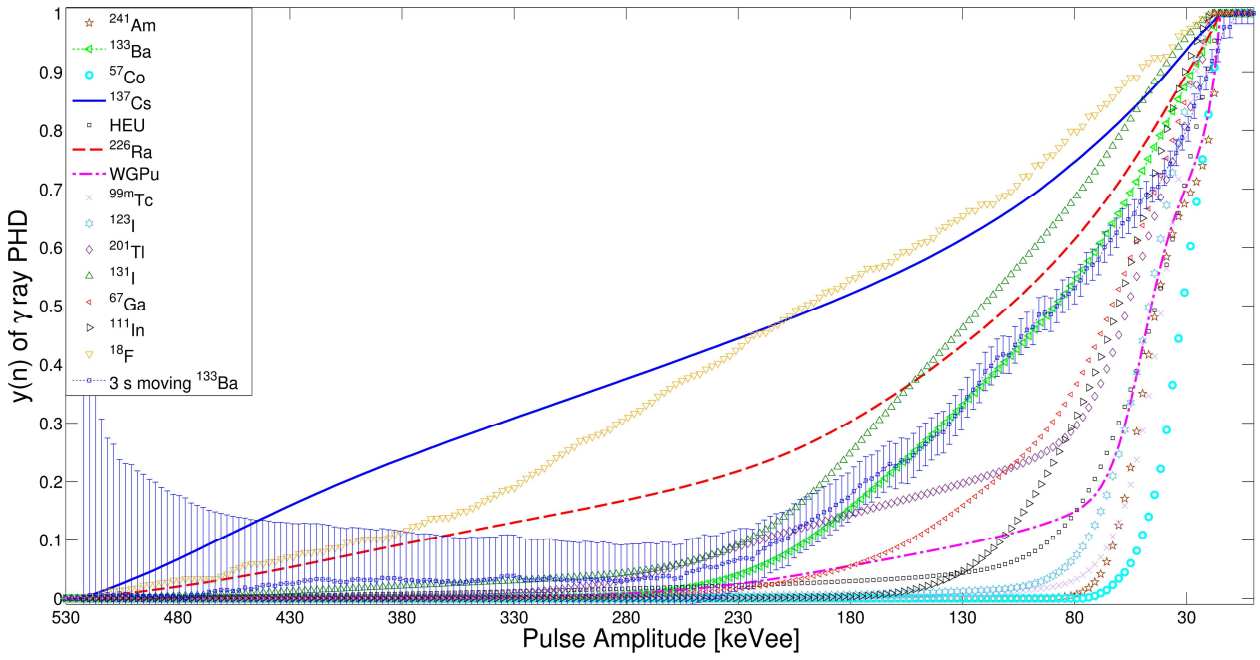
241Am
133Ba
57Co
137Cs
HEU
226Ra
WGPu
99mTc
123I
201Tl
131I
67Ga
111In
18F
3 s moving 133Ba
y(n) of γ ray PHD
Pulse Amplitude [keVee]
1
0.9
0.8
0.7
0.6
0.5
0.4
0.3
0.2
0.1
0
530
480
430
380
330
280
230
180
130
80
30

119

**(b)**

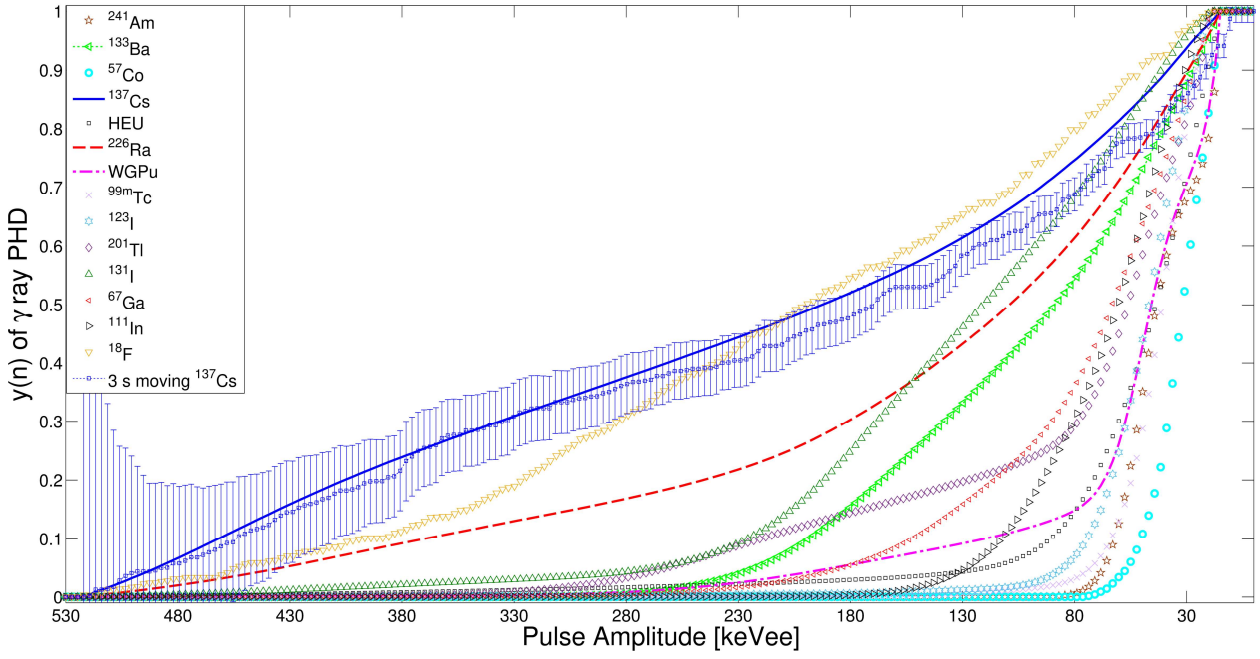
241Am
133Ba
57Co
137Cs
HEU
226Ra
WGPu
99mTc
123I
201Tl
131I
67Ga
111In
18F
3 s moving 137Cs
y(n) of γ ray PHD
Pulse Amplitude [keVee]
1
0.9
0.8
0.7
0.6
0.5
0.4
0.3
0.2
0.1
0
530
480
430
380
330
280
230
180
130
80
30

120

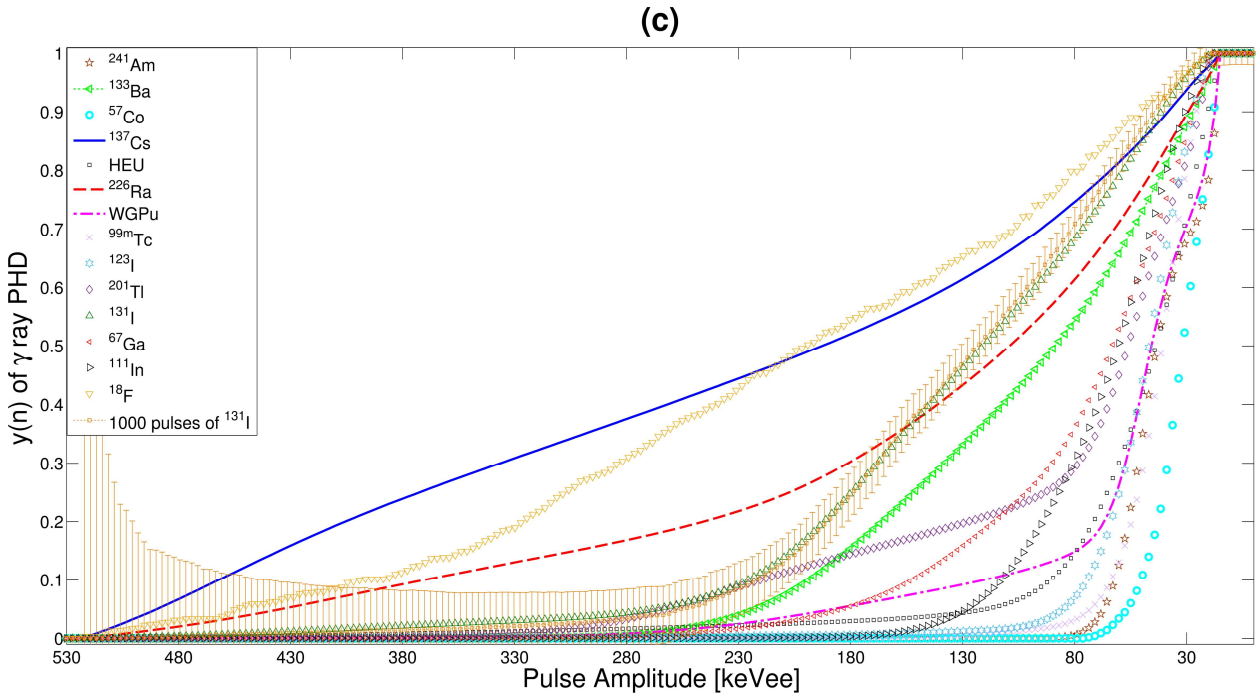


Figure 2: High-gain $y(n)$ library matrix for RPM radionuclide identification with $y(n)$ for gamma ray PHDs of moving measurements of (a) $^{133}$Ba, (b) $^{137}$Cs, (c) and $^{131}$I with pedestrian RPM at JRC Ispra, Italy, in February 2014 [26], and $y(n)$ of seven common medical isotopes measured at University of Michigan's C.S. Mott Children's Hospital in June 2016. Library matrix spectra generally exhibited a combined standard uncertainty below 0.1% due to the much longer measurement times relative to the three second moving source measurements, so error bars were excluded for the library spectra.

Visual comparisons of measured and reference $y(n)$ show that, for example, the $y(n)$ of the moving $^{137}$Cs and the $^{137}$Cs reference $y(n)$ behaving very similarly over the shown pulse height range. This trend, however, might not manifest itself in a point-by-point comparison of these $y(n)$, such as a least-squares comparison. A few outliers or detector gain shift could make a fit appear poor, even though visually a reference and measured $y(n)$ might agree well over most of the energy range. Therefore, we use a discrete Fourier transform (DFT) to convert $y(n)$ from the energy to the frequency domain. The Fourier transform will then describe how rapidly $y(n)$ changes over its domain, thus capturing information on its overall shape and behavior over its energy domain.

We use a fast Fourier transform (FFT) algorithm [32] to reduce the complexity of computing the DFT, as shown in Equation 1 below, for a vector of length N.

$$DFT(k) = \sum_{n=1}^{N} y(n) \exp\left(-i * 2 * \pi * (k-1) * \frac{n-1}{N}\right),\ 1 <= k <= N \qquad (1)$$

The absolute value of *DFT(k)* is the amount of frequency (Equation 2) in the signal, *y(n)* is $1 - x(n)$, *n* is the sample in the energy domain, and *k* is the sample in the frequency domain:

$$f = \frac{k-1}{N}. \quad (2)$$

For a continuous signal, the power spectral density (PSD), shown in Equation 3, computes how "power" is distributed over frequency of $y(n)$ by computing the square of the FFT:

$$PSD(k) = |FFT(k)|^2. \quad (3)$$

For RPMs, the "power" of the signal has no direct physical meaning, as it would in electrical engineering applications. Nevertheless, the power spectral density provides us with a metric for how measured and reference spectra behave over their entire domain.

## 2.3. Identifying radionuclides

We use spectral angle mapping (SAM) for comparing the modified measured RPM data from Section 2.2 to reference spectra. This method computes the spectral angle $\alpha_i$ between the measured and reference power spectral densities ($PSD(k)$ and $PSD_{matrix}(:, i)$), as shown in Equation 4 and Figure 3:

$$\alpha_i = \cos^{-1}\left[\frac{(PSD(k) \cdot PS\_matrix(:,i))}{\|PSD(k)\| \|PSD_{matrix}(:,i)\|}\right] \text{ [33]}. \quad (4)$$

This computation is performed point-by-point, and results in a spectral angle $\alpha$ in radians for each possible reference spectrum isotope *i* available in our library. The smaller the spectral angle, the better the fit is between a measured spectrum and that particular reference spectrum. Our algorithm selects the radionuclide with the reference spectrum that results in the lowest spectral angle $\alpha$ as a match to the measured spectrum. Section 3.2. includes a discussion on maximum possible $\alpha$-values and negative identifications.

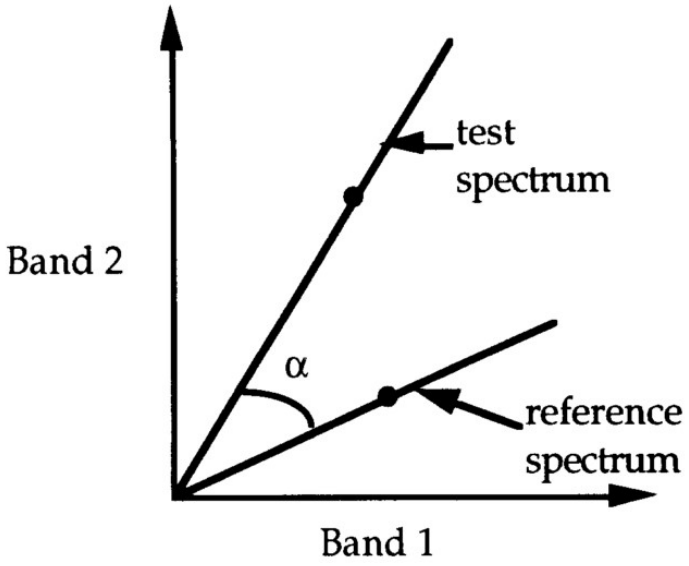


Figure 3: Illustration of spectral angle $\alpha$ that would be computed point by point between a measured spectrum and all possible reference spectra. The smallest total $\alpha$ indicates the best fit in the SAM analysis [33].

SAM was developed by J. W. Boardman in the early 1990s. The method's original application involved mapping the distribution and composition of materials on the earth's surface by comparing spectral similarities between measured and reference spectra from imaging spectrometry [33,34]. SAM has since been adopted for a variety of earth science applications for the purposes of spectral identification [35–38]. The SAM identification method has also been used in some limited fashions in nuclear sciences, but it has not yet been used for on-the-fly radionuclide identification with organic scintillators [39,40].

## 2.4. Comparison of radionuclide identification methods using F-scores

F-scores provide a statistical measure of radionuclide identification algorithm performances, while also factoring in a system's susceptibility to false negatives, i.e., not alarming on a present source [41]. The F-score ($F$) (Equation 5) utilizes both precision ($p$) and recall ($r$) values shown in Equations 6 and 7. Precision and recall values are based upon the system's true positive alarms or correct identifications ($t_p$), incorrect identifications or false positives ($f_p$), and not seeing a present source or false negatives ($f_n$):

$$F = \frac{(1+\beta^2)pr}{\beta^2 p + r}, \tag{5}$$

$$p = \frac{t_p}{t_P + f_p}, \tag{6}$$

$$r = \frac{t_p}{t_p + f_n}, \quad (7)$$

where $\beta$ is a weighting factor that can be used to emphasize the importance of precision (higher correct identification rate at cost of more false negatives) versus recall (lower false positive rate at cost of worse correct identification rate). A $\beta$ value of 1 indicates no bias towards either precision or recall. A perfect algorithm would result in an F-score of 1.

F-scores can be used to compare the performance of different radionuclide identification algorithms for a common dataset. Alternatively, one can apply one radionuclide identification algorithm to datasets of different levels of "difficulty" (more or fewer counts per spectrum), and then use F-score analysis to determine at what point an algorithm's failure rate becomes unacceptable.

# 3. Experimental Results

## 3.1. Experimental setup

Data used in the subsequent analysis were collected in two separate experiments. The full pedestrian RPM consisting of eight SCIONIX Holland model "76A76/3M-EJ309 E1XNEG" 7.6 cm diameter and 7.6 cm height cylindrical volume EJ309 organic liquid scintillation detectors was used to measure moving sources at a purpose-built RPM testing facility at the European Commission Joint Research Centre in Ispra, Italy, in February 2014 [22,24,26,28]. An electric rail-cart moved sources at a source height of 1.2 m and source transit speeds of 1.2 or 2.2 m/s. The perpendicular distance from the RPM front face and the source transit path was 1 m. The sources and source activities used in these measurements are given in Table 1. The table also lists source activities recommended by the ANSI standard for RPM testing [14]. The tests also included HEU and WGPu samples. The data acquisition time window was three seconds for all measurements.

Table 1: Sources available for RPM testing at JRC Ispra during February 2014 tests with pedestrian RPM [26]. Actual used source activities as well as ANSI-recommended source activities are listed [14].

| Source | Source Activity [kBq] (ANSI) [14] | Source Activity [kBq] (JRC Ispra 2/2014, pedestrian RPM) [26] |
|---|---|---|
| $^{57}$Co | 185 | 204 |
| $^{133}$Ba | 518 | 301 |
| $^{137}$Cs | 592 | 370 |
| $^{60}$Co | 259 | 259 |

| | | |
|---|---|---|
| $^{232}$Th | 517 | NA |
| $^{241}$Am | 1740 | 2220 |
| HEU | NA | 51 g; 89.9 % $^{235}$U |
| WGPu | NA | 6.6 g; 93% $^{239}$Pu |

Data were also acquired for common medical isotopes at the University of Michigan's C. S. Mott Children's Hospital in June 2016. Measurements were performed with a single 7.6 cm diameter cylindrical volume SCIONIX-Holland EJ309 organic liquid scintillation detector (see Figure 4), as well as three other organic scintillators that are not considered in the present analysis. The samples consisted of 260 kBq liquid solutions in glass vials. A list of medical isotopes measured, their activities at time of measurement, and their respective half-lives are listed in Table 2.

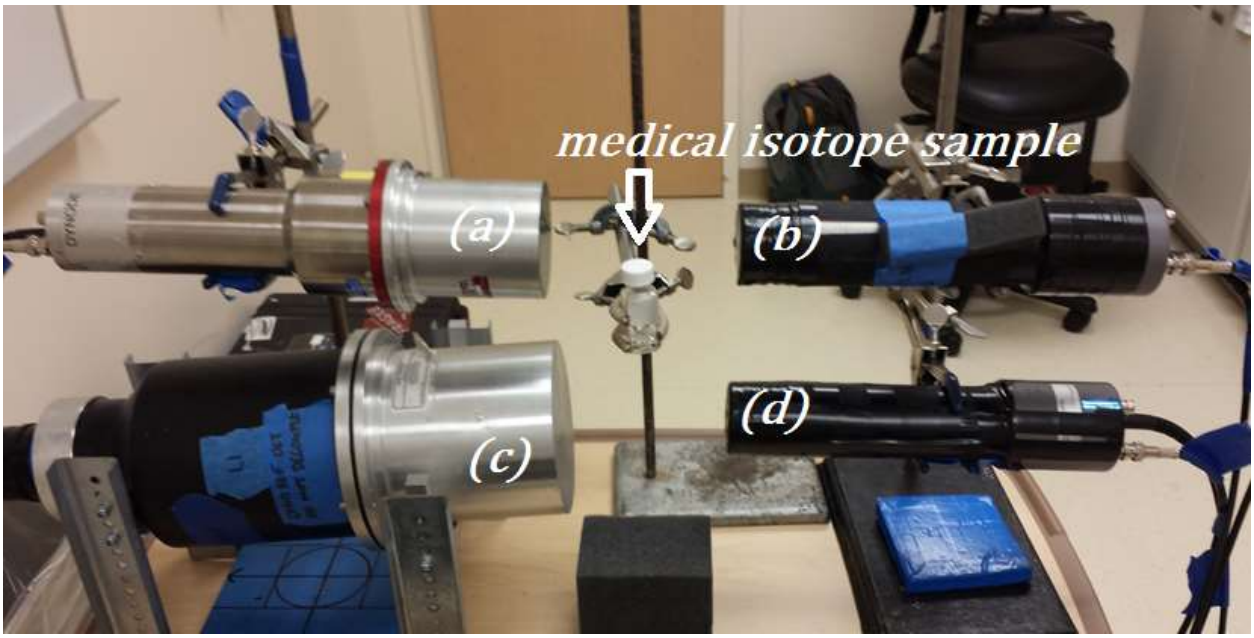


Figure 4: June 2016 setup for measuring medical isotopes at University of Michigan's C.S. Mott Children's Hospital using: (a) a 7.6 cm diameter by 7.6 cm height cylindrical volume EJ309 organic liquid scintillation detector, (b) stilbene crystal, (c) a larger organic liquid scintillation detector (d) a BB3 plastic scintillator from Radiation Monitoring Devices. (b-d) were not considered in present analysis.

Table 2: List of medical isotopes measured at University of Michigan's C.S. Mott Children's Hospital in June 2016 and their respective radioactive half-lives in hours, and their activities at time we measured them.

| Isotope | $T_{1/2}$ [h] | Activity at time of measurement [mCi] ±20% |
|---|---|---|
| $^{99m}$Tc | 6.0 | 0.007 |
| $^{123}$I | 13.3 | 0.007 |
| $^{201}$Tl | 72.9 | 0.008 |
| $^{131}$I | 192.5 | 0.008 |
| $^{111}$In | 67.3 | 0.007 |
| $^{18}$F | 1.8 | 0.001 |
| $^{67}$Ga | 78.3 | 0.007 |

Medical isotope samples were measured for thirty minutes each. Due to its short half-life, the $^{18}$F sample had substantially decayed by the time it was measured. However, because its half-life is so short, $^{18}$F is not considered a likely source of RPM nuisance alarms [21,19]. Therefore, the $^{18}$F results were excluded from the data analysis. The sources had 20% uncertainty in their calibrated activity. The source-to-detector distance was much shorter than that used for the pedestrian RPM, only one detector was used, and the source was static and not moving. Therefore, instead of trying to scale the medical isotope data to an expected response from the full pedestrian RPM, we used a fixed number of pulses sampled out of the thirty-minute measurement. This process was repeated to create the desired number of sample datasets for each medical isotope. For example, for the pedestrian RPM and the natural background radiation observed at the JRC Ispra, about 400 net counts after background subtraction were required to cause a gamma ray alarm. For the $^{99m}$Tc sample, we acquired thirty one-minute measurements. Data were down-sampled accordingly.

## 3.2. Radionuclide Identification Results for SAM

The radionuclide identification algorithm was tested on two datasets obtained with liquid organic scintillation detectors. The first, and less challenging dataset, henceforth named "Dataset 1", consists of thirty trials of three-second measurements of the sources listed in Table 1 travelling past the pedestrian RPM at 1.2 m/s [26]. Dataset 1 also includes thirty trials of 1,000 net pulses from the medical sources listed in Table 2. The more challenging second dataset, referred to

subsequently as "Dataset 2", uses pedestrian RPM measurements of the sources from Table 1 for which the source transit speed had been increased to 2.2 m/s. Dataset 2 also only uses 400 net pulses from the medical sources listed in Table 2.

Table 3 lists two parameters for each radionuclide from each of the two datasets. The first parameter of interest is whether or not enough gamma ray interactions were recorded to trigger a system alarm. In other words, does the RPM even register the presence of the source relative to natural background radiation? For Dataset 1 all sources are generally detected 100% of the time. For Dataset 2, however, the two lowest energy gamma ray emitting sources ($^{241}$Am, $^{57}$Co) are only detected approximately for half of the thirty trials per radionuclide.

The second parameter of interest concerns whether or not the RPM correctly identifies the source after the presence of a gamma ray source has been detected. From the Table 3 results, one again sees that this undertaking is easier with more counts per trial, i.e., the algorithm performs better for Dataset 1 as opposed to for Dataset 2. Assuming an average walking speed of 5 km/h (1.4 m/s), Dataset 1 is a more realistic dataset for a pedestrian RPM.

Tables 4 and 5 show the average SAM $\alpha$ values calculated for the correct radionuclide for the thirty trials per radionuclide from Datasets 1 and 2, respectively. Tables 4 and 5 also include the standard deviations of these SAM $\alpha$-values. A comparison of Tables 4 and 5 shows that Dataset 1 results in better, i.e., smaller, $\alpha$-values than those computed for Dataset 2.

$\alpha$-values are smaller on average for Dataset 1 versus Dataset 2 when considering the full results for 30 $^{99m}$Tc measurements for both Datasets 1 and 2, respectively. For Dataset 1, the SAM $\alpha$-values for comparisons with $^{99m}$Tc reference spectrum are mostly upwards of an order of five smaller than those for other possible radionuclide reference spectra. $^{123}$I results in a $y(n)$ very similar to that of $^{99m}$Tc, as shown in Figure 2. Nevertheless, the $\alpha$-values for the comparison with the $^{123}$I reference spectrum are still a factor of two larger than the $\alpha$-values for the comparisons with the $^{99m}$Tc reference spectrum. For Dataset 2, the $\alpha$-values for comparisons with the $^{99m}$Tc and $^{123}$I are more similar, which leads to two of 30 trials being misidentified as $^{123}$I.

Table 3: Results for pedestrian RPM alarming on different gamma ray sources and correctly identifying them with the SAM technique described in Section 2. Results are shown for two datasets described in Section 3.2. The first column per dataset lists the percentages out of 30 trials for which sufficient gamma rays above background were

detected to trigger an RPM alarm on the given source. The second column per dataset lists the percentages out of the number of gamma alarm cases for which correct radionuclide identification results were obtained.

| | Dataset 1 | | Dataset 2 | |
|---|---|---|---|---|
| Radionuclide | Gamma Alarm [%] | Correct ID [%] | Gamma Alarm [%] | Correct ID [%] |
| $^{57}$Co | 97% | 100% | 50% | 67% |
| $^{133}$Ba | 100% | 100% | 100% | 77% |
| $^{137}$Cs | 100% | 100% | 100% | 100% |
| $^{241}$Am | 100% | 100% | 60% | 94% |
| HEU | 100% | 100% | 100% | 60% |
| WGPu | 100% | 100% | 100% | 93% |
| $^{123}$I | 100% | 100% | 100% | 90% |
| $^{131}$I | 100% | 100% | 100% | 100% |
| $^{67}$Ga | 100% | 100% | 100% | 100% |
| $^{99m}$Tc | 100% | 100% | 100% | 93% |
| $^{201}$Tl | 100% | 100% | 100% | 100% |
| $^{111}$In | 100% | 100% | 100% | 100% |

Table 4: Average and standard deviations of the SAM $\alpha$-values computed for the correct isotope for thirty datasets for each of the 12 tested radionuclides (Dataset 1).

| | $^{241}$Am | $^{133}$Ba | $^{57}$Co | $^{137}$Cs | HEU | WGPu | $^{67}$Ga | $^{123}$I | $^{131}$I | $^{111}$In | $^{99m}$Tc | $^{201}$Tl |
|---|---|---|---|---|---|---|---|---|---|---|---|---|
| $\alpha_{avg}$ | 0.0061 | 0.0040 | 0.0065 | 0.0049 | 0.0047 | 0.0031 | 0.0018 | 0.0030 | 0.0016 | 0.0017 | 0.0020 | 0.0019 |
| $\alpha_{std}$ | 9.8E-04 | 5.2E-04 | 9.7E-04 | 5.3E-04 | 6.8E-04 | 3.9E-04 | 2.0E-4 | 3.3E-04 | 9.4E-04 | 2.0E-04 | 2.7E-04 | 1.9E-04 |

Table 5: Average and standard deviations of the SAM $\alpha$-values computed for the correct isotope for thirty datasets for each of the 12 tested radionuclides (Dataset 2). This number of counts is at the limit of detection for the pedestrian RPM for a three second measurement given the background conditions and associated gamma alarm threshold used at the JRC Ispra[26,31].

| | $^{241}$Am | $^{133}$Ba | $^{57}$Co | $^{137}$Cs | HEU | WGPu | $^{67}$Ga | $^{123}$I | $^{131}$I | $^{111}$In | $^{99m}$Tc | $^{201}$Tl |
|---|---|---|---|---|---|---|---|---|---|---|---|---|
| $\alpha_{avg}$ | 0.0072 | 0.0051 | 0.0076 | 0.0060 | 0.0062 | 0.0043 | 0.0034 | 0.0047 | 0.0030 | 0.0017 | 0.0037 | 0.0036 |
| $\alpha_{std}$ | 8.2E-04 | 6.9E-04 | 1.1E-03 | 5.0E-04 | 6.6E-04 | 5.6E-04 | 3.7E-4 | 4.9E-04 | 2.5E-04 | 2.0E-04 | 4.7E-04 | 3.7E-04 |

So far the $\alpha$-values have been presented as relative markers. However, even for some arbitrary input spectrum, the algorithm will still produce $\alpha$-values for the different radionuclides. These $\alpha$-values should be larger than if the spectra arose from the correct radionuclide source. Figure 5 shows three test cases, none of which should produce a positive identification as they include a background spectrum, a linear function, and a squared function. The $\alpha$-values obtained from the radionuclide identification algorithm using these datasets should provide a cutoff above which any $\alpha$-values can be considered proof of negative identification. The $\alpha$-values resulting

from these three test cases are shown in Table 6 and compared to results for WGPu measurements. The identification results for WGPu show much smaller $\alpha$-values than those for the three test cases from Figure 5, thus strengthening the plausibility that WGPu is present.

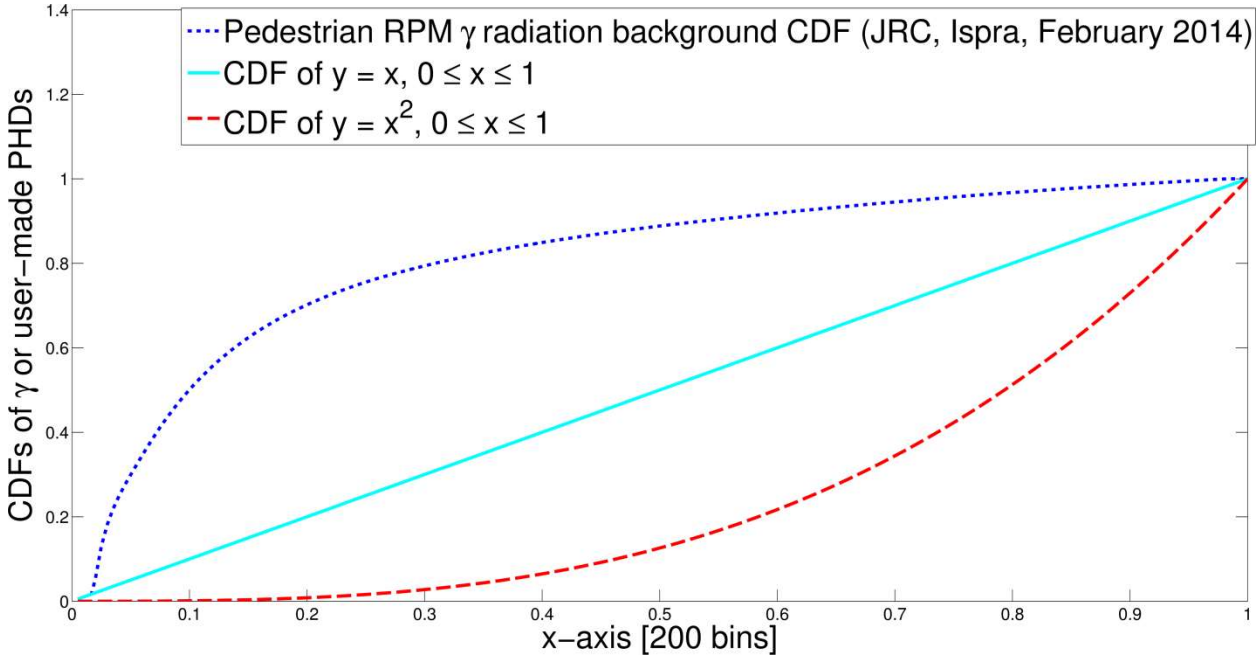


Figure 5: CDFs tested on power spectral density SAM radionuclide identification algorithm including CDFs of a gamma ray PHD background measurement, a linear function through the origin, and a square function through the origin. None of these functions should produce correct radionuclide source identifications. The SAM $\alpha$-values for these test cases are shown in Table 6.

Table 6: SAM $\alpha$-values computed for the test cases shown in Figure 5. None of these test cases are from actual sources, so they should not result in positive radionuclide identifications. The right most column shows SAM $\alpha$-values computed for actual WGPu measurements with the pedestrian RPM [26].

| Radionuclide | SAM $\alpha_{CDF_{BG}}$ | SAM $\alpha_{CDF_{y=x}}$ | SAM $\alpha_{CDF_{y=x^2}}$ | SAM $\alpha_{CDF_{WGPu_{avg}\pm WGPu_{stdev}}}$ |
|---|---|---|---|---|
| $^{241}$Am | 0.022 | 0.017 | 0.013 | 0.008±0.001 |
| $^{133}$Ba | 0.016 | 0.010 | 0.004 | 0.006±0.000 |
| $^{57}$Co | 0.020 | 0.014 | 0.009 | 0.005±0.001 |
| $^{137}$Cs | 0.012 | 0.004 | 0.004 | 0.009±0.001 |
| HEU | 0.020 | 0.014 | 0.008 | 0.005±0.001 |
| $^{226}$Ra | 0.014 | 0.007 | 0.003 | 0.007±0.001 |
| WGPu | 0.019 | 0.013 | 0.007 | 0.003±0.000 |
| $^{67}$Ga | 0.020 | 0.014 | 0.008 | 0.008±0.001 |
| $^{123}$I | 0.026 | 0.020 | 0.014 | 0.011±0.001 |
| $^{131}$I | 0.014 | 0.007 | 0.003 | 0.009±0.001 |
| $^{111}$In | 0.022 | 0.015 | 0.010 | 0.009±0.001 |
| $^{99m}$Tc | 0.028 | 0.022 | 0.016 | 0.013±0.001 |

| | | | | |
|---|---|---|---|---|
| $^{201}$Tl | 0.020 | 0.014 | 0.008 | 0.008±0.001 |

## 3.3. Comparison to Other Radionuclide Identification Algorithms

The performance of the radionuclide identification algorithm must be quantified with a metric that allows for easy comparisons with other identification algorithms. Table 7 gives F-score comparisons for the performance of the new and two previous identification algorithms [26,28] for Dataset 1. Each method clearly shows improved performance over the previous radionuclide identification algorithm.

Even the new radionuclide identification algorithm has its limitation though. Table 8 shows a slight dip in performance, as measured by the new F-score of 0.91, when the new algorithm is applied to the more challenging Dataset 2. Nevertheless, this F-score of 0.91 represents a significant improvement in performance over what either of the previously implemented identification algorithms achieved using the less challenging Dataset 1.

Table 7: Precision, recall, and F-scores computed for pedestrian RPM for Dataset 1 [26]. The following three isotope identification algorithms are compared: identification using least squares comparison with modified PHDs (LS PHD) [26,28], identification using least squares comparison with cumulative distribution functions (LS CDF) [26,31], and identification using power spectral density and spectral angular mapper (SAM-PSD) from Section 2 [31].

| | LS PHD | LS CDF | SAM-PSD |
|---|---|---|---|
| Precision | 0.58 | 0.70 | 1.0 |
| Recall | 0.99 | 0.99 | 1.0 |
| | | | |
| F($\beta$ = 1) | 0.73 | 0.82 | 1.0 |
| F($\beta$ = 0.5) | 0.63 | 0.74 | 1.0 |
| F($\beta$ = 2) | 0.87 | 0.92 | 1.0 |

Table 8: Precision, recall, and F-scores computed for Datasets 1 and 2 [26]. F-scores are computed for both datasets using the identification algorithm using power spectral density and spectral angular mapper from Section 2.

| | Dataset 1 | Dataset 2 |
|---|---|---|
| Precision | 1.0 | 0.90 |
| Recall | 1.0 | 0.92 |
| | | |
| F($\beta$ = 1) | 1.0 | 0.91 |
| F($\beta$ = 0.5) | 1.0 | 0.91 |

| | | |
|---|---|---|
| F($\beta$ = 2) | 1.0 | 0.91 |

## 4. Conclusions

Identifying and screening out nuisance alarms caused by NORM-bearing cargo and recent nuclear-medicine patients would result in significant time savings for RPM operators. Promising results were obtained for a new on-the-fly radionuclide identification algorithm on data obtained with an organic scintillator-based pedestrian RPM. Radionuclides measured included HEU and WGPu, common industrial sources, and several common medical isotopes.

The new algorithm emphasizes spectral characteristics by taking the power spectral density of modified CDFs of measured PHDs. This approach shows great sensitivity to trends in the measured data that are not apparent in the initial background corrected PHDs. A SAM method is used to compare measured and reference spectra, and thus determine a likeliest radionuclide match. F-score analysis shows a marked performance improvement from 0.82 to 1.0 for this new radionuclide identification algorithm over previous methods [26,28] when applied to the same datasets.

A successful and robust radionuclide identification algorithm for RPMs made of organic scintillators offers a way of reducing the number of nuisance alarms having to be processed in secondary inspections. Such a system could address the overwhelming ratio of nuisance to threat radiation alarms witnessed in RPMs. Future work will address scenarios including multiple sources present in a single measurement.

## 5. Acknowledgements

This research was performed under appointment to the Nuclear Nonproliferation International Safeguards Fellowship Program sponsored by the Nation Nuclear Security Administration's Office of International Nuclear Safeguards (NA-241).

It is also funded in-part by the Consortium for Verification Technology under Department of Energy National Nuclear Security Administration award number DE-NA0002534.

We would like to thank David Hubers and the University of Michigan's C. S. Mott Children's Hospital for providing a variety of medical isotopes for our experiments.

We would also like to thank Paolo Peerani and the European Commission Joint Research Centre in Ispra, Italy, for allowing our research group to participate in the 2014 SCINTILLA radiation portal monitor testing benchmarks.

We would also like to thank Richard Kouzes, Laboratory Fellow at Pacific Northwest National Laboratory, for his input and feedback on this work.

## 6. References

[1] Nuclear Security Summit, (n.d.). http://www.nss2016.org/.

[2] IAEA, Iaea Incident and Trafficking Database ( Itdb ), (2015). http://www-ns.iaea.org/downloads/security/itdb-fact-sheet.pdf.

[3] W.J. Broad, Seismic Mystery in Australia: Quake, Meteor or Nuclear Blast?, New York Times. (1997). http://www.nytimes.com/1997/01/21/science/seismic-mystery-in-australia-quake-meteor-or-nuclear-blast.html?pagewanted=all.

[4] R. Mowatt-Larssen, Al Qaeda Weapons of Mass Destruction Threat : Hype or Reality ?, Harvard Univ. Belfer Cent. Sci. Int. Aff. (2010). http://belfercenter.ksg.harvard.edu/publication/19852/al_qaeda_weapons_of_mass_destruction_threat.html.

[5] IAEA, IAEA Safety Standards: National Strategy for Regaining Control over Orphan Sources and Improving Control over Vulnerable Sources for protecting people and the environment (No. SSG-19 Specific Safety Guide), 2011. http://www-pub.iaea.org/MTCD/Publications/PDF/Pub1510_web.pdf.

[6] M. Castillo, Mexico issues alert after radioactive material stolen, CNN. (2016). http://www.cnn.com/2016/02/29/americas/mexico-radioactive-device-missing/.

[7] A. Rasheed, A. Mohammed, S. Kalin, Radioactive material stolen in Iraq raises security concerns, (2016). http://www.reuters.com/article/us-mideast-crisis-iraq-radiation-idUSKCN0VQ22F.

[8] R. Lee, Why Nuclear Smuggling Matters, Orbis. 52 (2008) 434–444. doi:http://dx.doi.org/10.1016/j.orbis.2008.05.007.

[9] V.D. Petrenko, Y.N. Karimov, A.I. Podkovirin, N.N. Shipilov, B.S. Yuldashev, M.I. Fazylov, Efforts of Uzbekistan to prevent nuclear terrorism and smuggling of radioactive and nuclear materials, Appl. Radiat. Isot. 63 (2005) 737–740. doi:10.1016/j.apradiso.2005.05.027.

[10] J.L. Jones, D.R. Norman, K.J. Haskell, J.W. Sterbentz, W.Y. Yoon, S.M. Watson, J.T. Johnson, J.M. Zabriskie, B.D. Bennett, R.W. Watson, C.E. Moss, J.F. Harmon, Detection of shielded nuclear material in a cargo container, Nucl. Instruments Methods Phys. Res. Sect. a-Accelerators Spectrometers Detect. Assoc. Equip. 562 (2006) 1085–1088. doi:10.1016/j.nima.2006.02.101.

[11] L. Lakosi, N.C. Tam, J. Zsigrai, Revealing smuggled nuclear material covered by a legitimate radioisotope shipment using CdTe-based gamma-ray spectrometry, Appl. Radiat. Isot. 58 (2003) 263–267. doi:10.1016/S0969-8043(02)00314-7.

[12] NNSA, National Nuclear Security Administration Second Line of Defense MEGAPORTS INITIATIVE, (2010). http://nnsa.energy.gov/sites/default/files/nnsa/inlinefiles/singlepages_9-15-2010.pdf.

[13] NNSA, Cooperative Border Monitoring Opportunities for the Global Partnership, (n.d.). http://www.state.gov/documents/organization/202455.pdf.

[14] ANSI, American National Standard for Evaluation and Performance of Radiation Detection Portal Monitors for Use in Homeland Security Accredited by the American National Standards Institute, 2007.

[15] PNNL, Radiation detectors at U.S. ports of entry now operate more effectively, efficiently, (2016). http://www.pnnl.gov/news/release.aspx?id=4245.

[16] Congress, SAFE Port Act, (2006). https://www.gpo.gov/fdsys/pkg/PLAW-109publ347/html/PLAW-109publ347.htm.

[17] R.T. Kouzes, J.R. Ely, A.T. Lintereur, D.L. Stephens, Neutron Detector Gamma Insensitivity Criteria. PNNL-18903, 2009.

[18] B.D. Geelhood, J.H. Ely, R.R. Hansen, R.T. Kouzes, J.E. Schweppe, R.A. Warner, Overview of Portal Monitoring at Border Crossings, in: Nucl. Sci. Symp. Conf. Rec. 2003 IEEE, 2004: pp. 513–517. doi:10.1109/NSSMIC.2003.1352095.

[19] R.T. Kouzes, E.R. Siciliano, The response of radiation portal monitors to medical radionuclides at border crossings, Radiat. Meas. 41 (2006) 499–512. doi:10.1016/j.radmeas.2005.10.005.

[20] R.T. Kouzes, J.H. Ely, A.T. Lintereur, E.K. Mace, D.L. Stephens, M.L. Woodring, Neutron detection gamma ray sensitivity criteria, Nucl. Inst. Methods Phys. Res. A. 654 (2011) 412–416. doi:10.1016/j.nima.2011.07.030.

[21] R.T. Kouzes, J.H. Ely, B.D. Geelhood, R.R. Hansen, E.A. Lepel, J.E. Schweppe, E.R. Siciliano, D.J. Strom, R.A. Warner, Naturally occurring radioactive materials and medical isotopes at border crossings, in: Nucl. Sci. Symp. Conf. Rec. 2003 IEEE, 2003: pp. 1448–1452. doi:10.1109/NSSMIC.2003.1351967.

[22] A. Sagadevan, M. Ruch, M.G. Paff, S.D. Clarke, S. a. Pozzi, Simulation of an EJ-309 Based Pedestrian Radiation Portal Monitor using MCNPX-PoliMi, in: Proc. 55th Annu. Meet. Inst. Nucl. Mater. Manag. July 20-24, 2014, 2014.

[23] M. Ruch, M. Paff, A. Poitrasson-Riviere, A. Sagadevan, S.D. Clarke, S.A. Pozzi, P. Peerani, Large volume organic liquid scintillation detectors as a vehicle radiation portal monitor prototype at the 3rd SCINTILLA benchmark campaign, in: Proc. 56th Annu. Meet. Inst. Nucl. Mater. Manag. July 12-16, 2015, 2015.

[24] M. Paff, M. Ruch, A. Sagadevan, S.D. Clarke, S.A. Pozzi, P. Peerani, Performance of a EJ309 organic liquid scintillation detector pedestrian radiation portal monitor prototype at the 2nd SCINTILLA benchmark campaign, in: Proc. 55th Annu. Meet. Inst. Nucl. Mater. Manag. July 20-24,

2014, 2014.

[25] M.G. Paff, S.D. Clarke, S.A. Pozzi, Organic liquid scintillation detector shape and volume impact on radiation portal monitors, Nucl. Instruments Methods Phys. Res. Sect. A Accel. Spectrometers, Detect. Assoc. Equip. 825 (2016) 31–39. doi:10.1016/j.nima.2016.03.102.

[26] M.G. Paff, M.L. Ruch, A. Poitrasson-Riviere, A. Sagadevan, S.D. Clarke, S. Pozzi, Organic liquid scintillation detectors for on-the-fly neutron/gamma alarming and radionuclide identification in a pedestrian radiation portal monitor, Nucl. Inst. Methods Phys. Res. A. 789 (2015) 16–27. doi:10.1016/j.nima.2015.03.088.

[27] M.G. Paff, S.D. Clarke, S.A. Pozzi, Optimization of organic liquid scintillation detectors in radiation portal monitor applications, in: IEEE Symp. Radiat. Meas. Appl. May 22-26, 2016, Berkeley, CA, USA, 2016.

[28] M.L. Ruch, M. Paff, A. Sagadevan, S.D. Clarke, S.A. Pozzi, Radionuclide Identification by an EJ309 Organic Scintillator - Based Pedestrian Radiation Portal Monitor Using a Least Squares Algorithm, in: Proc. 55th Annu. Meet. Inst. Nucl. Mater. Manag. July 20-24, 2014, 2014.

[29] J.K. Polack, M. Flaska, A. Enqvist, C.S. Sosa, C.C. Lawrence, S.A. Pozzi, An algorithm for charge-integration, pulse-shape discrimination and estimation of neutron/photon misclassification in organic scintillators, Nucl. Instruments Methods Phys. Res. Sect. A Accel. Spectrometers, Detect. Assoc. Equip. 795 (2015) 253–267. doi:10.1016/j.nima.2015.05.048.

[30] J.C.F.G.I.M. JCGM, Evaluation of measurement data — Guide to the expression of uncertainty in measurement, Int. Organ. Stand. Geneva ISBN. (2008). doi:10.1373/clinchem.2003.030528.

[31] M. Paff, Reducing medical isotope nuisance alarms in radiation portal monitors, in: Consort. Verif. Technol. Work., Ann Arbor, MI, 2016. http://cvt.engin.umich.edu/wp-content/uploads/sites/173/2016/07/Poster14-Paff-20161010_CVT_Poster_PAFF.pdf.

[32] G.D. Bergland, A guided tour of the fast Fourier transform, IEEE Spectr. 6 (1969) 41–52. doi:10.1109/MSPEC.1969.5213896.

[33] F.A. Kruse, A.B. Lefkoff, J.W. Boardman, K.B. Heidebrecht, A.T. Shapiro, P.J. Barloon, A.F.H. Goetz, The Spectral Image Processing System (SIPS) Interactive Visualization and Analysis of Imaging Spectrometer Data, Remote Sens. Environ. 44 (1993) 145–163. doi:10.1016/0034-4257(93)90013-N.

[34] R.H. Yuhas, A.F.H. Goetz, J.W. Boardman, Discrimination among semi-arid landscape endmembers using the Spectral Angle Mapper (SAM) algorithm, in: JPL, Summ. Third Annu. JPL Airborne Geosci. Work. Vol. 1 AVIRIS Work., 1992: pp. 147–149. http://ntrs.nasa.gov/archive/nasa/casi.ntrs.nasa.gov/19940012238.pdf.

[35] Y. Sohn, N.S. Rebello, Supervised and unsupervised spectral angle classifiers, Photogramm. Eng. Remote Sensing. 68 (2002) 1271–1280.

[36] E.L. Hunter, C.H. Power, An assessment of two classification methods for mapping Thames Estuary intertidal habitats using CASI data, Int. J. Remote Sens. 23 (2002) 2989–3008. doi:10.1080/01431160110075596.

[37] X. Zhang, P. Li, Lithological mapping from hyperspectral data by improved use of spectral angle mapper, Int. J. Appl. Earth Obs. Geoinf. 31 (2014) 95–109. doi:10.1016/j.jag.2014.03.007.

[38] H. Yagoub, A.H. Belbachir, N. Benabadji, Detection and mapping vegetation cover based on the Spectral Angle Mapper algorithm using NOAA AVHRR data, Adv. Sp. Res. 53 (2014) 1686–1693. doi:10.1016/j.asr.2014.03.020.

[39] M.S. Bandstra, T.J. Aucott, E. Brubaker, D.H. Chivers, R.J. Cooper, J.C. Curtis, J.R. Davis, T.H. Joshi, J. Kua, R. Meyer, V. Negut, M. Quinlan, B.J. Quiter, S. Srinivasan, A. Zakhor, R. Zhang, K. Vetter, RadMAP: The Radiological Multi-sensor Analysis Platform, Nucl. Instruments Methods Phys. Res. Sect. A Accel. Spectrometers, Detect. Assoc. Equip. 840 (2016) 59–68. doi:10.1016/j.nima.2016.09.040.

[40] L. Caneve, F. Colao, R. Fantoni, L. Fiorani, Scanning lidar fluorosensor for remote diagnostic of surfaces, Nucl. Instruments Methods Phys. Res. Sect. A Accel. Spectrometers, Detect. Assoc. Equip. 720 (2013) 164–167. doi:10.1016/j.nima.2012.12.009.

[41] M. Sokolova, G. Lapalme, A systematic analysis of performance measures for classification tasks, Inf. Process. Manag. 45 (2009) 427–437. doi:10.1016/j.ipm.2009.03.002.